Journal Pre-proof

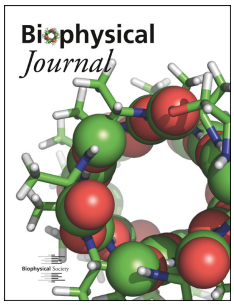

Nano-compartmentalization of the nuclear pore lumen

Kai Huang, Mario Tagliazucchi, Sung Hyun Park, Yitzhak Rabin, Igal Szleifer

PII: S0006-3495(19)30947-6

DOI: https://doi.org/10.1016/j.bpj.2019.11.024

Reference: BPJ 9967

To appear in: *Biophysical Journal*

Received Date: 25 July 2019

Accepted Date: 18 November 2019

Please cite this article as: Huang K, Tagliazucchi M, Park SH, Rabin Y, Szleifer I, Nano-compartmentalization of the nuclear pore lumen, *Biophysical Journal* (2019), doi: https://doi.org/10.1016/j.bpj.2019.11.024.

Nano-compartmentalization of the nuclear pore lumen

Kai Huang[1], Mario Tagliazucchi[2], Sung Hyun Park[1], Yitzhak Rabin[3], and Igal Szleifer[1,4,5*]

[1]Department of Biomedical Engineering, Northwestern University, Evanston, IL 60208, United States
[2]DQIAQF and INQUIMAE, Facultad de Ciencias Exactas y Naturales, Universidad de Buenos Aires, Ciudad Universitaria, Pab. II, C1428EHA, Ciudad Autónoma de Buenos Aires, Argentina
[3]Department of Physics and Institute for Nanotechnology and Advanced Materials, Bar-Ilan University, Ramat-Gan 52900, Israel
[4]Department of Chemistry, and Chemistry of Life Processes Institute, Northwestern University, Evanston, IL 60208, United States
[5]Chemistry of Life Processes Institute, Northwestern University, Evanston, IL 60208, United States

*To whom correspondence may be addressed. E-mail: igalsz@northwestern.edu.

Abstract: The nuclear pore complex (NPC) employs the intrinsically disordered regions (IDRs) from a family of phenylalanine-glycine-rich nucleoporins (FG-Nups) to control nucleocytoplasmic transport. It has been a long-standing mystery how the IDR-mediated mass exchange can be rapid yet selective. Here, we use a computational microscope to show that nano-compartmentalization of IDR subdomains leads to a remarkably elaborate gating structure as programmed by the amino-acid sequences. In particular, we reveal a heterogeneous permeability barrier that combines an inner ring barrier with two vestibular condensates. Throughout the NPC, we find a polarized electrostatic potential and a diffuse thermoreversible FG-network featuring mosaic FG-territories with low FG-FG pairing fraction. Our theoretical anatomy of the central transporter sheds lights into the sequence-structure-function relationship of the FG-Nups and provides a picture of nucleocytoplasmic mass exchange that allows a reconciliation of transport efficiency and specificity.

Statement of Significance: Structural knowledge of the nuclear pore complex is crucial for understanding the nucleocytoplasmic transport and the assembly of large molecular machineries. Despite extensive study, the nuclear pore complex lumen assembled by intrinsically disordered proteins is still poorly understood. Here, we show that this functional core of the nuclear pore complex is more structured than previously pictured. We found that the sequences of the disordered proteins guide them to organize into a remarkable nano-gate featuring (1) heterogeneous entropic barrier, (2) polarized electrostatic potential, and (3) distinct functional

territories. Our insights from the nuclear pore complex open up new paradigms for macromolecule design and artificial molecular assembly.

Introduction

As the largest cellular channel, the nuclear pore complex (NPC) mediates the biomass transport between nucleus and cytoplasm with high selectivity and efficiency. Unlike mechanical or motor-driven biological nanochannels that undergo stimuli-responsive conformational transitions between open and closed states for gating, NPC has a relatively static scaffold[1,2] constituted by the folded domains of hundreds of nucleoporins (Nups), and employs the intrinsically disordered regions (IDRs) of a subset of these Nups as its gatekeepers. Such IDRs form the central transporter[1,3,4], a selective permeability barrier that has been a long-standing black box due to the difficulty of experimental visualization[5–10]. Within the yeast nuclear pore of 40nm width (about 2 times the resolution of the state-of-the-art fluorescence microscopy) reside more than 10 different types and more than 200 copies of IDRs. Termed as FG-Nups, the gating biopolymers use their phenylalanine-glycine (FG) repeat motifs to interact with nuclear transport receptors (NTRs), which facilitate the transport of macromolecules that carry specific labels (short peptides that serve as nuclear import/export signals)[11–13].

The FG-Nups in vitro undergo phase separation to form nonstoichiometric hydrogel[14,15] that behaves like a hydrophobic sieve[16,17,14,18,19]. This behavior is typical of associative polymers interacting by the pairing of sticker groups[20]. In the case of FG-Nups, the stickers are the hydrophobic FG repeats interspersed by hydrophilic spacers. However, whether gelation of FG-Nups happens in vivo under the stoichiometric and geometrical constraints imposed by the scaffold is highly controversial. Recent experiments suggested that the permeability barrier is more than a hydrophobic sieve[21,22], with highly dynamic FG-Nups in vivo[23,24] that are more like a polymer brush as envisioned by the virtual gating hypothesis[25–28]. However, in this gel-brush debate, the diversity of IDRs inside the nuclear pore is overlooked. As shown in Fig. 1A, B, the FG-IDRs differ greatly not only in stoichiometry and length, but also in grafting address and amino-acid code. A closer look of the protein sequences reveals that many IDRs have well-defined subdomains that are enriched in either non-cohesive charged spacers (amino-acid code DEKR) or cohesive neutral spacers[15] (amino-acid code NQT). To further decipher the IDR codes, we classify the large family of FG motifs into three generic groups: 1) single FG motifs, 2) FG motifs with neighboring hydrophobic groups such as GLFG, xAFG, xIFG, and 3) FG motifs with separated

hydrophobic groups such as FxFG, LSFG, ISFG (x indicates neutral hydrophilic amino acids only, since neighboring charged amino acids are expected to suppress hydrophobicity[29]). Under such classification, we find type-2 FG motifs to be remarkably enriched inside the cohesive subdomains whereas type-3 FG motifs reside largely inside the non-cohesive subdomains. Together, these observations strongly suggest that the NPC lumen is not a homogeneous permeability barrier but may further compartmentalize into fine gating structures. Beyond the brush-vs-gel dichotomy, qualitative hybrid models based on in vitro characterization of individual FG-Nups have been proposed[30,31], yet a consensus on the in vivo picture has not been reached. To answer the question how nucleocytoplasmic transport is rapid yet selective, quantitative understanding of the permeability barrier based on integrative characterization of the FG-Nups as a whole is needed.

As one of the earliest attempts to build a comprehensive molecular theory of the nuclear pore lumen, our previous study predicted a toroidal cloud of IDRs that has a higher density near the NPC scaffold than along the pore axis[32]. This picture is in line with another comprehensive theoretical study[33] based on coarse-grained molecular dynamics (MD) simulations. Although the qualitative agreement between two different methods is encouraging, both models do not discriminate between different transport hypotheses and cannot explain many recent experimental findings. It is also worth noting that the pore geometry and stoichiometry of the FG-Nups in previous models were based on experimental data about the NPC scaffold that is now out of date. Recent experiments reveal that the NPC scaffold consists of three[1], rather than four rings[34], with the inner ring structure well preserved from yeast to human cells[2]. For the yeast NPC, the stoichiometry (copy numbers of FG-Nups in the NPC) had nearly doubled in recent experimental reports compared with previous ones[1,35]. The implementation of such an experimental update is necessary for a faithful description of the central transporter by quantitative models.

Here, we build upon our previous work a new NPC model with significant improvements in 1) the geometry of the scaffold, 2) the stoichiometry and anchoring positions of the IDRs, 3) the description of molecular interactions, and 4) the differentiation between various FG motifs (see the Methods section for more details). To our best knowledge, our new NPC model is the first one that implements the state-of-the-art experimental data, considers full amino-acid sequences of the IDRs, and addresses the interplay between various protein interactions. Our model shows that the

complex interplay between FG-IDRs, including hydrophobic interaction, specific spacer cohesion, volume exclusion, and charge effect, leads to a remarkably elaborate gating structure inside the nuclear pore. In particular, we find spatial segregation between cohesive and non-cohesive regions, and a polarized electrostatic potential throughout the NPC. The model predicts a thermoreversible FG-network featuring mosaic FG-territories, i.e., distinct territories of different types of FG motifs. Our results highlight nano-compartmentalization of IDR subdomains as an important mechanism in shaping the central transporter of the NPC. Protein phase separation has been recently recognized as an important driving force in the formation of membraneless organelles. Unlike liquid-liquid phase separation that drives membraneless compartmentalization[36–40], the predicted nano-condensates in the nuclear pore are constrained by the NPC scaffold and programmed by the sequences of the FG-Nups. Such sequence-programmed "nanophase separation" reconciles a wide array of existing experimental observations and explains how nucleocytoplasmic transport can be efficient yet specific. These insights on the sequence-structure-function relationship of FG-Nups can be used to engineer functional phase separation of sequence-controlled synthetic polymers[41–43] and to build smart artificial nanopores[44–51].

Methods

We have constructed an NPC-specific model based on a molecular theory[52] with the free energy functional of the system written in general terms as:

$$F = -TS + E_{\text{elec}} + E_{\text{vdW}} + E_{\text{pairing}} + F^{\text{mix}}_{\text{acid-base}} \quad (1)$$

The first term on the right-hand side of Eq. 1 includes the translational entropies of solvent molecules, cations, anions, protons and hydroxyl ions, and the conformational entropy of the IDRs. The model inputs a large set of molecular conformations of the IDRs so that their conformational entropy can be evaluated to be $\sum_\alpha P(\alpha)\ln(\alpha)$, where $P(\alpha)$ is the probability of a disordered protein being in conformation α. Based on the conformational probability, we construct the spatial density fields of various molecular species and calculate their electrostatic (E_{electro}), van der Waals (E_{vdW}), and hydrophobic pairing (E_{pairing}) energies from a mean field approach. The last term of Eq.

1 accounts for the local acid-base equilibrium of the amino acids. The model explicitly takes into account the amino-acid sequences of the IDRs. We classified all the amino acids into 10 groups according to their hydrophobicity, charge, cohesiveness, and acid-base properties. For simplicity, we coarse-grained the NPC scaffold into three tori as shown in Fig. 1B.

The stoichiometry of the FG-Nups and the anchoring positions of their IDRs are based on experimental studies of the NPC scaffold. Aware of the uncertainty and controversy in the copy number and anchoring position of some FG-Nups, we have chosen the most recent experimental data[1,35] and made educated guesses for the uncertain ones as input of our model. We also developed a new theoretical description of the hydrophobic pairing interaction between the FG repeats that enables the present model to examine the possibility of gelation of FG-Nups *in vivo* by calculating the pairing fraction of FG motifs in space. We have carried out MD simulation to show that Phe-Phe pairing energy (between single-molecule amino acids) is around 2.5kT in water at 300K (Fig. S1). Although estimating this pairing energy from the simulation depends on the choice of force field[24,53], we found 2.5kT a reasonable estimate and a useful parameterization guideline in our model. While this number might be slightly inflated, one should keep in mind that the presence of multivalent NTRs in the NPC (not explicitly included in our model) could effectively enhance the pairing strength between the FG repeats. Besides FG-pairing, we also assigned 1kT attraction between the NQT spacers, as they were revealed by experiments to be more cohesive than other spacers[15]. The combination of two distinct interactions allows the new model to explore a wide spectrum of possible morphologies from brush to hydrogel and test different structural hypotheses. To this end, we have explored a wide range of energy parameters to gain a comprehensive understanding of the effect of protein interaction on the gating structure of the NPC. More details of the model and its numerical solution can be found in the supplemental material.

Results and Discussions

Interplay of FG-pairing and specific spacer attraction in shaping the central transporter

Mounting evidence suggests that FG-FG pairing and spacer interactions are weak in nature[23,54,24], i.e., their strengths are not much higher than the thermal energy kT. However, given the

uncertainty of the interaction strengths, it is instructive to systematically study the molecular organization of FG-IDRs under various arbitrary combinations of the FG-pairing and spacer cohesiveness. As shown in Fig. 1F, when all the cohesive interactions are turned off, the overall spatial distribution of the IDRs is highly diffuse with the density of amino acids being lower along the pore axis than near the scaffold where the IDRs are anchored. Increasing the FG-pairing strength (Fig. 1D, E) and the spacer cohesiveness (Fig. 1G, H) contracts the FG-Nups into the central barrier zone encircled by the inner scaffold ring (location marked in Fig. 1B), where gelation is expected to happen according to the selective phase hypothesis[18]. Notably, the predicted condensation is rather limited if one of the two cohesive forces is weak, in line with in vitro experimental observations that both FG-pairing and attractive spacer interaction are indispensable for enabling gel-like barrier structures[15,30,55]. However, we found that even with both relatively strong FG-pairing (2.5kT) and spacer attraction (1kT), i.e., condition for Fig. 1C, the central barrier does not seal itself and leaves open a narrow axial conduit. Such unoccluded barrier structure that protrudes from the inner ring is similar to that found in electron microscopy (EM) experiments[56], and is consistent with the single-molecule super-resolution fluorescence observation of a single central channel for passive diffusion of small molecules[57]. However, one should keep in mind that the experimental evidence is controversial since the EM map lacks information about the central axis of the NPC and the pathways revealed by single-molecular imaging depend on rather optimisticassumptions about the resolution[58].

Outside the central barrier, our model predicts that the synergy between FG pairing and cohesive spacers can lead to two high-density condensates (marked in Fig. 1C), reminiscent of recent EM studies where the central transporter appears as a two-lobed blur[1]. The condensation of FG-IDRs at the two exits of the pore implies that the functional gate of NPC is not limited to the central barrier but extends to the cytoplasmic and the nuclear sides. In particular, the prediction of a prominent cohesive zone at the cytoplasmic vestibule of the NPC suggests that molecular screening for nuclear import may take place before the cargoes reach the central barrier of NPC. Apart from the condensed zones, the overall spatial distribution of FG-IDRs is diffuse enough to create a highly dynamic FG cloud encapsulating the central barrier, in accord with the atomic force microscopy (AFM) observations[59] of large structural variance of the FG-IDRs looking from the cytoplasmic side of NPC. It is worth noting that the vestibular condensation of FG-IDRs at the

cytoplasmic exit of the pore requires strong cohesiveness to compensate for the conformational entropy penalty associated with the stretching of these IDR. Compared to the ring barrier near the scaffold, the vestibular condensates are more sensitive to the degree of FG crosslinking. Therefore, such condensation might not be prominent without the aid of multivalent NTRs that can bind to multiple FG motifs. In line with the above consideration, a recent AFM study reported that Impβ facilitates the occlusion of the cytoplasmic side of NPC[60]. There are also experimental reports of two pools of NTRs at the vestibules of the pore with the concentration at cytoplasmic side being higher[61,62]. The pooling of the NTRs has been explained by low density brushes of FG-Nups at the vestibules of the pore[61]. Our model suggests an alternative picture in which the NTR pooling is associated with vestibular condensation. Note that while the long cohesive FG-Nups (Nup116, Nup100) anchored at the cytoplasmic side can extend into the nuclear pore and seal the central barrier in conjunction with short cohesive FG-Nups (Nup57, Nup49) that emanate from the inner ring, this would involve a conformational entropy penalty and is therefore unlikely, as indicated by our model in which both energy and conformational entropy considerations are quantitatively taken into account. The short FG-Nups alone cannot occlude the entire central barrier zone due to the geometrical constraints, in line with recent experiments on artificial nanopores that mimic the NPC[63]. The predicted complex density profile of the IDRs suggests that the entropic barrier for nucleocytoplasmic mass exchange is inhomogeneous in the space of the NPC. Such a heterogeneous permeability barrier is expected to entropically select and steer the passage of biomolecules in a size-dependent manner through steric interaction.

Thermoreversible FG-network and polarized electrostatic potential

In Fig. 1C we have shown how a heterogeneous central transporter emerges under FG (2.5kT) and spacer (1kT) cohesive interactions. In the remainder of the paper, we focus on this reasonably cohesive case and visualize its fine structure from a diversity of perspectives that the model provides, starting with the spatial distributions of FG repeats. As shown in Fig. 2A, our model predicts a diffuse yet inhomogeneous spatial distribution of FG repeats (see Fig. S2D for non-Phenylalanine hydrophobic amino acids). The FG concentration reaches around 40 mM inside the condensed domains and drops to 10-30 mM outside them. The overall FG concentration is lower than the ~50 mM saturation limit suggested by in vitro experiments[17], but it is significantly higher

than the estimates (<10 mM) from super-resolution fluorescence experiment[64]. Even for the non-cohesive system that features a brush-like morphology, we found an average FG concentration in the range of 20-30 mM (Fig. S3B). If the current estimates of the stoichiometry of FG-Nups are reliable[1,35], the average concentration cannot be much lower than that, due to the confinement imposed by the scaffold. This means that the average FG concentration is not sensitive to whether the morphology of the central transporter is brush-like or gel-like. The quantity that truly distinguishes the two cases is the degree of crosslinking of the FG-Nups[18] which can be quantified by the fraction of FG motifs that are paired up. Such FG-pairing fraction depends not only on the FG concentration but also on the FG interaction strength, and can go from nearly none (completely non-cohesive) to almost 100% (saturated pairing).

Fig. 2B shows our theoretical predictions for the FG-pairing fraction throughout the NPC. On average the pairing fraction is around 30%, which is an order of magnitude higher than that obtained for a non-cohesive system (~3%, Fig. S3C). This number, however, is well below the saturation limit assumed in the selective phase model[17], which means there are many (~70%) dangling FG motifs that are ready to bind with NTRs. In a sense, the thermoreversible FG-network predicted by our model is in an intermediate state between a brush and a gel, with both brush and gel characteristics to some degree. The pairing fraction is not homogeneous and exhibits a spatial pattern that overlaps with the FG-rich domains in Fig. 2A, reflecting the fact that FG-pairing tends to condense FG motifs. Moreover, regions rich in FG motifs and high pairing fraction roughly coincide with domains rich in cohesive NQT spacers (Fig. 2C), highlighting again the important role of these spacers in shaping the central transporter. Like Fig. 1C, Figs. 2A-C also reveal the existence of two vestibules at both the cytoplasmic and the nuclear sides that are rich in FG motifs and cohesive spacers, which could recruit Impβ1 at both exits of the central pore, as observed in experiments[61,62]. In our recent theoretical study of the transport pathways of model cargoes through a cylindrical nanochannel coated with homopolymers, we found that the cargoes with moderate polymer affinity tend to accumulate near the two vestibules of the channel, due to the substantially larger accessible volume (and therefore larger entropy) for both the cargoes and the polymers[65]. The shape of the NPC scaffold with widely open exits and the deployment of long FG-Nups at the outer rings suggest that a pooling mechanism (vestibular accumulation for efficient

transport) has been exploited and optimized in the nucleocytoplasmic transport. Such pooling of NTRs could in return strengthen the vestibular barriers to block unrecognized macromolecules.

In addition to the thermoreversible FG-network, we predict a net positive charge homogeneously distributed throughout most of the central transporter (except near the cytoplasmic ring, see Fig. 2D), with an average net charge concentration of about 20 mM. Such positively charged nano-environment is electrostatically favorable for macromolecules that are negatively charged, consistent with the prior finding that NTRs and NTR-cargo complexes bear more negative charges than most cellular proteins[66]. To better understand the electrostatics of the NPC, we calculated the electrostatic potential produced by the charged FG-Nups. As shown in Fig. 2E, the overall potential is positive as expected based on the net charge distribution. However, it is intriguing that this self-built potential is highly inhomogeneous and asymmetric in space. Compared to the relatively weak and uniform potential in the pore center, the potential near the scaffold is both intensified and polarized. In particular, a negative potential appears near the cytoplasmic ring and transitions into positive potential near the inner ring and the nuclear ring. The roughly 1 mV difference between the inner scaffold ring and the axis of the pore is expected to provide an electrostatic energy bonus of about 2kT for the NTRs of average charge around -50e, to follow a peripheral pathway near the inner ring. This could explain fluorescence and EM observations of NTRs such as Impβ1, NTF2, Kap104 and Kap121 near the periphery of the pore[57,67,68], and fluorescence observations that positively charged cargoes pass the NPC along the axial channel[64]. Note that the observation of peripheral translocation of NTRs is counterintuitive from an entropic perspective, since the existence of the central ring barrier (Fig. 1C) is expected to expel the macromolecules away from the peripheral region due to steric interaction. The peripheral preference of NTRs is also hard to explain from a FG-binding argument, given the relatively homogeneous distribution of FG motifs in the central barrier (Fig. 2A).

Our prediction that the inhomogeneous electrostatic potential is not correlated with the density profile of the IDRs highlights electrostatic steering as an additional path-selective mechanism to the entropic steering for the nucleocytoplasmic transport. We propose that the center-to-periphery electrostatic potential gradient participates in dispersing cargoes according to their

charge to size ratios. The functional role of the negative potential near the cytoplasmic ring is not entirely clear at present but it is likely to assist with NTR pooling before nuclear import and to direct the negatively charged cargoes to the central ring. It is worth noting that the polarized electrostatic potential arises not only due to the net charge distribution but also due to the inhomogeneous osmotic pressure inside NPC. In fact, in stark contrast to the net charge distribution, the distribution of charged amino acids DEKR (see Figs. S2A, B for their positive and negative partitions) has a highly inhomogeneous spatial pattern (Fig. 2F), in remarkable anti-correlation with the neutral cohesive spacers (Fig. 2C). Such "nanophase separation" between the charge-rich non-cohesive and the charge-poor cohesive regions inside the nuclear pore creates a complex nano-environment within the nuclear pore to house distinct pathways for different cargoes.

It is worth noting that the cohesive phase, despite its higher amino-acid density, is still rich in water and dangling FG motifs, and therefore should not be confounded with an oil-like hydrophobic phase or a hydrogel phase. The constraints of stoichiometry and geometry imposed by the NPC scaffold also limit the size of the cohesive condensates to the nanoscale, which is smaller than most of the membrane-less compartmentalization in biological systems. While both the FG-pairing and specific spacer attraction contribute to the cohesiveness of the condensates, they shape the morphology of the central transporter in disparate ways as shown in Fig. S4. More specifically, very strong FG-pairing interaction in the absence of spacer attraction homogenizes the IDR spatial distribution by forming a more saturated FG-network without distinguishable ring barrier and vestibular condensates. On the contrary, significant spacer attraction without FG-pairing collapses the IDRs into a highly heterogeneous structure.

Mosaic FG-territories and an atlas of individual FG-Nups

Figs. 2A, B depict a thermoreversible FG-network where unpaired FG motifs are widely dispersed and available for binding of NTRs throughout the NPC. However, at this point it is still unclear how such a diffuse cloud of FG motifs directs the traffic through the lumen of the NPC. To shed more light on this issue, we distinguish between three generic types of FG motifs as shown in Fig. 1A. The spatial distributions of the three types of FG motifs are shown in Figs. 3A-C. It is interesting

that the different FG motifs form distinct nano-domains in space. The single FG motifs are concentrated along the axis of the pore (Fig. 3A), filling the low-density axial conduit we showed in Fig. 1C, which could explain the experimental finding that the central channel for the passive diffusion of small molecules is more viscous than an open aqueous conduit[57]. The central and the cytoplasmic barriers are enriched predominantly by type-2 FG motifs (Fig. 3B), whereas most type-3 FG motifs (Fig. 3C) are widely distributed outside the barriers. Figs. 3E, F show the spatial distributions of GLFG, FxFG, the most-studied type-2 and type-3 FG motifs, which are clearly segregated from each other. The spatial distribution of other FG motifs (non-GLFG-FxFG) is peaked about the axis of the NPC, similarly to the single FG motifs (Fig. 3D). The complementary nano-domains of distinct FG motifs are expected to add on the entropic and electrostatic steering another layer of pathway specificity[69] for multivalent NTRs and their cargo-complexes to undergo path-selective transport.

Since all FG motifs have similar pairing energy in our model, the nano-compartmentalization of different FG motifs is a unique biological "phase separation" that is programmed into the amino-acid sequences of the FG-Nups. Different from the macro-phase separation, here the "phases" are limited to nano-scale. One could argue that such a nano-structure could be "smeared out" by thermal fluctuations but since our model describes the time-averaged structure at thermodynamic equilibrium and incorporates the effects of thermal fluctuations of the IDRs through the conformational entropy of the polymers, we believe that the emerging mosaic picture of the special organization of FG motifs is robust. Under our FG classification protocol, subdomains of type-2 and type-3 FG-motifs can be clearly seen in the color-coded sequences shown in Fig. 1A. Moreover, the two types of subdomains have distinct concentrations of cohesive spacers (purple) and charges (orange). It is well known from in vitro experiments that GLFG-rich Nups such as Nup116, Nup100, Nup57, Nup49 contain most cohesive subdomains[30] that are vital for forming the permeability barrier. Recent experiments reveal that GLFG-motifs directly bind to multiple scaffold Nups and that the GLFG-rich long Nup116 and Nup100 play important roles in the biogenesis of the NPC[70]. In our model, we have assigned weak interactions between the inner surface of the coarse-grained scaffold and all the FG-Nups. In line with the experimental observations, we predict that GLFG-rich Nups are localized in the vicinity of the scaffold and constitute the cohesive central barrier (Fig. 3G). Remarkably, our model predicts that long

Nup116 and Nup100 form a cytoplasm-oriented structure, analogous to the nuclear basket but much more disordered. The overall spatial distribution of the cohesive FG-Nups is also cytoplasm-oriented, suggestive of a potential role of the spatial gradient of type-2 FG-motifs in guiding nuclear export. Interestingly, it has been observed by super-resolution imaging that Nup116 segment as a cargo[64] (which can homotypically interact with GLFG-Nups) and mRNA during export[71] both have a similar spatial pattern with high dwelling probability in the central barrier ring and the cytoplasmic vestibule. On the other hand, the larger amount of type-3 FG motifs within the nuclear half of the NPC suggests that their spatial gradient could direct nuclear import, in line with reports that FxFG motifs are stronger binders to the hydrophobic pockets of Impβ than GLFG motifs[72]. Fig. 3H presents the spatial distribution of non-cohesive FG-Nups, which shows up in the periphery of the cytoplasmic half and fills the nuclear half of NPC. The partially cohesive Nsp1, with non-cohesive FxFG-rich subdomain near the anchoring end and cohesive subdomain near the free end, fills the central lumen of the NPC, while depleted from the scaffold and the central barrier (Fig. 3I).

Fig. 4 shows an atlas of 11 types of individual FG-Nups. The cytoplasm-oriented, center-oriented and nucleoplasm-oriented FG-Nups are displayed in the upper, middle and lower rows, respectively. The spatial distributions of the FG-Nups along the axis of the pore are largely determined by their anchor positions. The central FG-Nups have more copy numbers than the cytoplasmic and nuclear ones. Among them, the Nup49 and Nup57 are short in length and constitute the high-density central ring rich in GLFG motifs. On the cytoplasmic side, Nup116 and Nup100 participate in forming the cytoplasmic barrier of the pore whereas Nup159 and Nup42 reside at the pore periphery, consistent with the experimental observation that Nup116 and Nup100 contribute more to the NPC permeability barrier than other FG-Nups[73]. Note that while Nup116 has both swollen and collapsed subdomains, the collapse of its cohesive subdomain tends to happen near the pore axis. Nup159 carries more negative charges than positive ones and contributes to the negative electrostatic potential shown in Fig. 2E. It is interesting to observe how these highly charged long FG-Nups extend into the cytoplasmic side like antennas. In a non-cohesive system (Fig. S3D), Nup116 and Nup100 do not block the cytoplasmic side and have a peripheral distribution like that of Nup159. Near the nucleoplasmic side, the FG-Nups also differ in

their lengths and spatial distributions. The long IDRs of Nup1 and Nup2 are enriched in type-3 FG motifs, in contrast to the short IDRs of Nup145N, Nup60 that carry mostly type-2 FG motifs. It is worth noting that, except for the most abundant Nsp1, all the FG-Nups have localized spatial distributions and are characterized by specific FG motifs. The lack of overlap between the cytoplasm- and nucleoplasm-oriented FG-Nups suggests that nucleocytoplasmic transport necessitates switching between different FG-Nups by a sequence of binding and unbinding events. An alternative translocation picture is the Brownian ratchet model[74,75], in which a cargo remains bound to the same FG-Nup, translocating via Brownian motion biased by a chemical potential gradient, until its release. While our model does not exclude the possibility of such single-Nup "ferry" events, we expect them to be rare based on the territorial picture that emerges from our model, according to which different IDRs are localized in different parts of the pore. Our model, however, delineates a highly heterogenous picture of the nuclear lumen, where the Brownian motion of cargoes will be guided not only by the spatial gradients of different FG groups with different binding affinities, but also by the density gradient of the FG-Nups (that act as crowders) and by the gradient of the electrostatic potential.

The whole is more than the sum of its parts

The current advances in revealing the structure of the NPC scaffold have been based on a divide-and-conquer methodology which breaks this structure into subcomplexes that can be analyzed at atomic resolution using protein crystallization and then integrated back to get the whole picture. Can we apply an analogous approach to understand the functional core, i.e., the central transporter of the NPC?

To answer this question, we studied a reference system where isolated IDRs are characterized individually and superposed to construct an overall gating structure. In other words, the cross-interactions between different IDRs are turned off in this reference system. Fig. 5A shows the overall gating structure of the reference system and a few typical spatial distributions of the isolated IDRs. Since most of the FG-Nups have anchoring positions within 20nm of the pore equator (Fig. 1B), the reference system has a concentrated IDR distribution inside the central barrier zone and near the inner ring of the scaffold. However, compared to the fully interacting

system (Fig. 1C, color panel), it lacks the vestibular condensates at the exits of the pore, suggesting that the formation of vestibular barriers/recruiters necessitates the interplay between different FG-Nups, and especially the volume exclusion between different IDR territories (Fig. 4). In the fully interacting system, the spatial distributions of long FG-Nups such as Nup100, Nup116, Nup159, Nup1 and Nup2 are extended towards either the cytoplasmic or the nuclear side of the NPC depending on their anchoring positions (Fig. 3G, H, Fig. 4), whereas Nsp1 with anchoring positions across the pore equator have polarized distributions that are depleted around the central barrier ring (Fig. 3I, Fig. 4). In the reference system, these FG-Nups in their isolated states tend to occupy the NPC lumen in a less segregated way (Fig. 5A). Among all the isolated FG-Nups, Nup116 are predicted to form the largest condensate along the pore axis (Fig. 5A), consistent with their leading role in NPC biogenesis. Compared to the fully interacting system (Fig. 2), the reference system has drastically different spatial distributions of the cohesive (NQT) and charged (DEKR) spacers (Fig. 5B, C), with no sign of "phase separation" between them. The net charge of FG-Nups is less homogeneously distributed (Fig. 5D) and the electrostatic potential is more intensified in the central barrier (Fig. 5E). The reference system has a more concentrated distribution of all the FG motifs and has more intermixed domains of distinct FG motifs (Fig. 5F-I), compared to the fully interacting system (Fig. 2A, Fig. 3A-C). These comparisons highlight the importance of cross-interaction between FG-Nups in forming the extensive and intricate gating structure of NPC, which demonstrates that the central transporter as a whole is more than the sum of the parts. Consistent with deletion experiments[76], our result suggests that deleting a sufficiently large number of FG-Nups in the pore will affect the overall function, even if those FG-Nups are not directly involved in the transport mechanism for a given NTR.

Conclusion and outlook

In this work, we have studied a molecular model that provides high-resolution structural details about the distribution of intrinsically disordered regions (IDRs) inside the NPC. Our results reveal an intricate integration of various FG-Nups, resulting in an elaborate central transporter. Besides a high-density FG-ring at the equator of the pore that has been reported in previous models[32,33], our work suggests the existence of vestibular condensates along the axis of pore that can serve as barriers for inert molecules and as attractors for FG binders. However, we find the vestibular

condensates to be more sensitive to the FG crosslinking than the ring barrier is. This is due to the higher entropic cost of condensation at the vestibules of the pore than that at the peripheral ring near the inner scaffold. The same entropic reason explains why the long Nup116 and Nup100 do not seal the center barrier of the pore with the shorter Nup57 and Nup49, but rather form a barrier structure at the cytoplasmic side of the pore. It is possible that NTRs are needed to elicit or stabilize the predicted cytoplasmic barrier structure[60]. Such picture is in accord with the experimentally observed pooling of NTRs[61,62], which could in return strengthen the distal barriers at the pore exits. Nevertheless, since the loading condition of the pore is likely time-dependent, the vestibular condensation is expected to be subject to temporal fluctuations.

Our analysis highlights the importance of the cohesive domains laden with specific attractive spacers (NQT) in guiding the self-assembly of FG-Nups in vivo into segregated cohesive and non-cohesive zones with the latter being rich in charges. However, even inside the cohesive region we find the pairing fraction of FG motifs to be less than 50%, meaning there exist more dangling than paired FG motifs. In concord with recent experimental finding[30], we predict that FG-Nups that are rich in cohesive subdomains, such as Nup116, Nup100, Nup57, Nup49 and Nup145N, dominate the proximity of the NPC scaffold and are crucial to the permeability barrier. However, the overall spatial distribution of the FG-Nups is predicted to remain diffuse in the cytoplasmic side, meaning the cytoplasmic part of the NPC is highly flexible and dynamic, in line with AFM observations[59]. By classifying the FG motifs into three generic groups, we find the cohesive subdomains to be rich in type-2 FG motifs with neighboring hydrophobic amino acids, such as GLFG, xAFG, xIFG. While it is well known that GLFG are crucial for the cohesiveness of FG-Nups, more experimental efforts are needed to investigate whether other type-2 FG-motifs facilitate barrier formation and NPC biogenesis.

Our model reveals an intensified and polarized electrostatic field near the NPC scaffold. The highly positive potential near the inner ring provides an electrostatic explanation for the experimental finding that negatively charged NTRs tend to shuttle near the NPC scaffold[57,67,68] whereas positive cargoes are confined to the axial channel[64]. On the other hand, the unoccluded central barrier predicted by our model is consistent with the experimental observation that passive diffusion of small cargoes takes an axial pathway[57]. The thermoreversible FG-network predicted by our model

features complementary nano-domains of different FG motifs, implying their distinct functions in the selective barrier. The compartmentalization of FG motifs is encoded in the amino-acid sequences of the IDRs and in the anchoring addresses at which they emanate from the scaffold and does not incur significant conformational entropy penalty for the FG-Nups. However, we show that interactions between different FG-Nups are necessary to orchestrate and sustain such mosaic FG-territories.

We propose that the combination of entropic, electrostatic, and FG steering mechanisms allows the central transporter of NPC to control the pathways of cargoes according to their size, charge, and FG-affinity. The steric interaction between a heterogeneous entropic barrier and a cargo is expected be sensitive to the size of the cargo. In our recent theoretical study, we found that entropic effects drive large cargoes to take a more centralized pathway through a polymer-coated nanochannel, and to pool at the channel exits due to balance of entropic penalty and cargo-polymer affinity[65]. The pooling mechanism could accelerate the tunneling of large cargoes through NPC. Besides steric interaction, electrostatics and FG-binding are two other important factors that influence the path-selective transport. Along their peripheral pathway favored by the electrostatic interaction, the NTRs will likely need to transition between the FxFG and GLFG domains, with small energetic gain or loss through multivalent weak hydrophobic interactions. Such multivalent targeting scenario has been recently shown to enable high molecular sensitivity and specificity compared to strong monomeric binding[69]. For NTRs that have a higher affinity to FxFG than to GLFG, for example Impβ as suggested by literature[72], passing through the GLFG ring will have counteracting energetic effects from FG-binding and electrostatic interaction that permit fast trafficking, whereas NTRs that are more GLFG-philic could be trapped near the scaffold. More systematic experimental investigation on the specific NTR-FG interactions is needed towards a full picture of path selectivity.

In summary, by accounting for high-resolution sequences, comprehensive molecular interactions and their coupling, our model provides a picture of the ultrastructure of FG-Nups that could lend explanations to a wide array of existing experimental observations. Our theoretical anatomy of the NPC lumen suggests a possible reconciliation between high efficiency and high specificity of

nucleocytoplasmic transport by predicting: 1) a diffuse thermoreversible (weakly and partially cross-linked) FG-network with widely available dangling FG motifs for fast NTR binding and unbinding, 2) a heterogeneous permeability barrier with a polarized electrostatic potential and mosaic FG-territories that enables path-selective transport on the basis of entropic, electrostatic, and FG steering. These results shed light on the sequence-structure-function relationship of the unfolded FG-Nups, which can be tested by new experiments. Future modeling efforts will be directed towards the study of transport dynamics through the predicted NPC structure.

Acknowledgements: IS, KH gratefully acknowledge funding from NSF Biol & Envir Inter of Nano Mat 1833214, and NIH National Cancer Institute R01 CA228272. YR would like to acknowledge support by grants from the Israel Science Foundation and from the Israeli Centers for Research Excellence program of the Planning and Budgeting Committee. We thank Dr. André Hoelz and Dr. Barak Raveh for discussion of the NPC scaffold.

Author contributions: Conceptualization, K.H., Y.R., and I.S.; Methodology, K.H.; Software, K.H., M.T., and S.H.P.; Formal Analysis, K.H.; Investigation, K.H.; Writing-Original Draft, K.H.; Writing-Review & Editing, K.H., Y.R., M.T., S.H.P., and I.S.; Supervision, Y.R., and I.S.; Project Administration, I.S.; Funding Acquisition, Y.R., and I.S.

Declaration of interests: The authors declare no competing interests.

References

(1) Kim, S. J.; Fernandez-Martinez, J.; Nudelman, I.; Shi, Y.; Zhang, W.; Raveh, B.; Herricks, T.; Slaughter, B. D.; Hogan, J. A.; Upla, P.; et al. Integrative Structure and Functional Anatomy of a Nuclear Pore Complex. *Nature* **2018**, *555* (7697), 475–482. https://doi.org/10.1038/nature26003.

(2) Lin, D. H.; Stuwe, T.; Schilbach, S.; Rundlet, E. J.; Perriches, T.; Mobbs, G.; Fan, Y.; Thierbach, K.; Huber, F. M.; Collins, L. N.; et al. Architecture of the Symmetric Core of the Nuclear Pore. *Science* **2016**, *352* (6283), aaf1015–aaf1015. https://doi.org/10.1126/science.aaf1015.

(3) Yang, Q.; Rout, M. P.; Akey, C. W. Three-Dimensional Architecture of the Isolated Yeast Nuclear Pore Complex: Functional and Evolutionary Implications. *Mol. CELL* **1998**, *1* (2), 223–234. https://doi.org/10.1016/S1097-2765(00)80023-4.

(4) Beck, M. Nuclear Pore Complex Structure and Dynamics Revealed by Cryoelectron Tomography. *Science* **2004**, *306* (5700), 1387–1390. https://doi.org/10.1126/science.1104808.

(5) Lowe, A. R.; Siegel, J. J.; Kalab, P.; Siu, M.; Weis, K.; Liphardt, J. T. Selectivity Mechanism of the Nuclear Pore Complex Characterized by Single Cargo Tracking. *NATURE* **2010**, *467* (7315), 600–603. https://doi.org/10.1038/nature09285.

(6) Szymborska, A.; de Marco, A.; Daigle, N.; Cordes, V. C.; Briggs, J. A. G.; Ellenberg, J. Nuclear Pore Scaffold Structure Analyzed by Super-Resolution Microscopy and Particle Averaging. *Science* **2013**, *341* (6146), 655–658. https://doi.org/10.1126/science.1240672.

(7) von Appen, A.; Beck, M. Structure Determination of the Nuclear Pore Complex with Three-Dimensional Cryo Electron Microscopy. *J. Mol. Biol.* **2016**, *428* (10), 2001–2010. https://doi.org/10.1016/j.jmb.2016.01.004.
(8) Musser, S. M.; Grunwald, D. Deciphering the Structure and Function of Nuclear Pores Using Single-Molecule Fluorescence Approaches. *J. Mol. Biol.* **2016**, *428* (10), 2091–2119. https://doi.org/10.1016/j.jmb.2016.02.023.
(9) Jovanovic-Talisman, T.; Zilman, A. Protein Transport by the Nuclear Pore Complex: Simple Biophysics of a Complex Biomachine. *Biophys. J.* **2017**, *113* (1), 6–14. https://doi.org/10.1016/j.bpj.2017.05.024.
(10) Thevathasan, J. V.; Kahnwald, M.; Cieśliński, K.; Hoess, P.; Peneti, S. K.; Reitberger, M.; Heid, D.; Kasuba, K. C.; Hoerner, S. J.; Li, Y.; et al. Nuclear Pores as Versatile Reference Standards for Quantitative Superresolution Microscopy. *Nat. Methods* **2019**, *16* (10), 1045–1053. https://doi.org/10.1038/s41592-019-0574-9.
(11) Görlich, D.; Kutay, U. Transport Between the Cell Nucleus and the Cytoplasm. *Annu. Rev. Cell Dev. Biol.* **1999**, *15* (1), 607–660. https://doi.org/10.1146/annurev.cellbio.15.1.607.
(12) Stewart, M. Molecular Mechanism of the Nuclear Protein Import Cycle. *Nat. Rev. Mol. Cell Biol.* **2007**, *8* (3), 195–208. https://doi.org/10.1038/nrm2114.
(13) Köhler, A.; Hurt, E. Exporting RNA from the Nucleus to the Cytoplasm. *Nat. Rev. Mol. Cell Biol.* **2007**, *8* (10), 761–773. https://doi.org/10.1038/nrm2255.
(14) Frey, S.; Görlich, D. FG/FxFG as Well as GLFG Repeats Form a Selective Permeability Barrier with Self-Healing Properties. *EMBO J.* **2009**, *28* (17), 2554–2567. https://doi.org/10.1038/emboj.2009.199.
(15) Ader, C.; Frey, S.; Maas, W.; Schmidt, H. B.; Goerlich, D.; Baldus, M. Amyloid-like Interactions within Nucleoporin FG Hydrogels. *Proc. Natl. Acad. Sci. U. S. A.* **2010**, *107* (14), 6281–6285. https://doi.org/10.1073/pnas.0910163107.
(16) Ribbeck, K.; Gorlich, D. Kinetic Analysis of Translocation through Nuclear Pore Complexes. *EMBO J.* **2001**, *20* (6), 1320–1330. https://doi.org/10.1093/emboj/20.6.1320.
(17) Frey, S.; Görlich, D. A Saturated FG-Repeat Hydrogel Can Reproduce the Permeability Properties of Nuclear Pore Complexes. *Cell* **2007**, *130* (3), 512–523. https://doi.org/10.1016/j.cell.2007.06.024.
(18) Hülsmann, B. B.; Labokha, A. A.; Görlich, D. The Permeability of Reconstituted Nuclear Pores Provides Direct Evidence for the Selective Phase Model. *Cell* **2012**, *150* (4), 738–751. https://doi.org/10.1016/j.cell.2012.07.019.
(19) Schmidt, H. B.; Görlich, D. Transport Selectivity of Nuclear Pores, Phase Separation, and Membraneless Organelles. *Trends Biochem. Sci.* **2016**, *41* (1), 46–61. https://doi.org/10.1016/j.tibs.2015.11.001.
(20) Semenov, A. N.; Rubinstein, M. Thermoreversible Gelation in Solutions of Associative Polymers. 1. Statics. *Macromolecules* **1998**, *31*, 1373–1385. https://doi.org/10.1021/ma970616h.
(21) Kroschwald, S.; Maharana, S.; Simon, A. Hexanediol: A Chemical Probe to Investigate the Material Properties of Membrane-Less Compartments. *Matters* **2017**. https://doi.org/10.19185/matters.201702000010.
(22) Rog, O.; Köhler, S.; Dernburg, A. F. The Synaptonemal Complex Has Liquid Crystalline Properties and Spatially Regulates Meiotic Recombination Factors. *eLife* **2017**, *6*. https://doi.org/10.7554/eLife.21455.
(23) Hough, L. E.; Dutta, K.; Sparks, S.; Temel, D. B.; Kamal, A.; Tetenbaum-Novatt, J.; Rout, M. P.; Cowburn, D. The Molecular Mechanism of Nuclear Transport Revealed by Atomic-Scale Measurements. *eLife* **2015**, *4*. https://doi.org/10.7554/eLife.10027.
(24) Raveh, B.; Karp, J. M.; Sparks, S.; Dutta, K.; Rout, M. P.; Sali, A.; Cowburn, D. Slide-and-Exchange Mechanism for Rapid and Selective Transport through the Nuclear Pore Complex. *Proc. Natl. Acad. Sci. U. S. A.* **2016**, *113* (18), E2489–E2497. https://doi.org/10.1073/pnas.1522663113.
(25) Rout, M. P.; Aitchison, J. D.; Suprapto, A.; Hjertaas, K.; Zhao, Y. M.; Chait, B. T. The Yeast Nuclear Pore Complex: Composition, Architecture, and Transport Mechanism. *J. CELL Biol.* **2000**, *148* (4), 635–651. https://doi.org/10.1083/jcb.148.4.635.
(26) Rout, M. P.; Aitchison, J. D.; Magnasco, M. O.; Chait, B. T. Virtual Gating and Nuclear Transport: The Hole Picture. *TRENDS CELL Biol.* **2003**, *13* (12), 622–628. https://doi.org/10.1016/j.tcb.2003.10.007.
(27) Lim, R. Y. H.; Huang, N.-P.; Koser, J.; Deng, J.; Lau, K. H. A.; Schwarz-Herion, K.; Fahrenkrog, B.; Aebi, U. Flexible Phenylalanine-Glycine Nucleoporins as Entropic Barriers to Nucleocytoplasmic Transport. *Proc. Natl. Acad. Sci.* **2006**, *103* (25), 9512–9517. https://doi.org/10.1073/pnas.0603521103.
(28) Wente, S. R.; Rout, M. P. The Nuclear Pore Complex and Nuclear Transport. *Cold Spring Harb. Perspect. Biol.* **2010**, *2* (10), a000562–a000562. https://doi.org/10.1101/cshperspect.a000562.
(29) Huang, K.; Gast, S.; Ma, C. D.; Abbott, N. L.; Szlufarska, I. Comparison between Free and Immobilized Ion Effects on Hydrophobic Interactions: A Molecular Dynamics Study. *J. Phys. Chem. B* **2015**, *119* (41), 13152–13159. https://doi.org/10.1021/acs.jpcb.5b05220.

(30) Patel, S. S.; Belmont, B. J.; Sante, J. M.; Rexach, M. F. Natively Unfolded Nucleoporins Gate Protein Diffusion across the Nuclear Pore Complex. *CELL* **2007**, *129* (1), 83–96. https://doi.org/10.1016/j.cell.2007.01.044.
(31) Yamada, J.; Phillips, J. L.; Patel, S.; Goldfien, G.; Calestagne-Morelli, A.; Huang, H.; Reza, R.; Acheson, J.; Krishnan, V. V.; Newsam, S.; et al. A Bimodal Distribution of Two Distinct Categories of Intrinsically Disordered Structures with Separate Functions in FG Nucleoporins. *Mol. Cell. PROTEOMICS* **2010**, *9* (10), 2205–2224. https://doi.org/10.1074/mcp.M000035-MCP201.
(32) Tagliazucchi, M.; Peleg, O.; Kröger, M.; Rabin, Y.; Szleifer, I. Effect of Charge, Hydrophobicity, and Sequence of Nucleoporins on the Translocation of Model Particles through the Nuclear Pore Complex. *Proc Natl Acad Sci USA* **2013**, *110*, 3363–3368. https://doi.org/10.1073/pnas.1212909110.
(33) Ghavami, A.; Veenhoff, L. M.; van der Giessen, E.; Onck, P. R. Probing the Disordered Domain of the Nuclear Pore Complex through Coarse-Grained Molecular Dynamics Simulations. *Biophys. J.* **2014**, *107* (6), 1393–1402. https://doi.org/10.1016/j.bpj.2014.07.060.
(34) Alber, F.; Dokudovskaya, S.; Veenhoff, L. M.; Zhang, W.; Kipper, J.; Devos, D.; Suprapto, A.; Karni-Schmidt, O.; Williams, R.; Chait, B. T.; et al. The Molecular Architecture of the Nuclear Pore Complex. *NATURE* **2007**, *450* (7170), 695–701. https://doi.org/10.1038/nature06405.
(35) Rajoo, S.; Vallotton, P.; Onischenko, E.; Weis, K. Stoichiometry and Compositional Plasticity of the Yeast Nuclear Pore Complex Revealed by Quantitative Fluorescence Microscopy. *Proc. Natl. Acad. Sci.* **2018**, *115* (17), E3969–E3977. https://doi.org/10.1073/pnas.1719398115.
(36) Brangwynne, C. P.; Tompa, P.; Pappu, R. V. Polymer Physics of Intracellular Phase Transitions. *Nat. Phys.* **2015**, *11* (11), 899–904. https://doi.org/10.1038/nphys3532.
(37) Wu, H.; Fuxreiter, M. The Structure and Dynamics of Higher-Order Assemblies: Amyloids, Signalosomes, and Granules. *Cell* **2016**, *165* (5), 1055–1066. https://doi.org/10.1016/j.cell.2016.05.004.
(38) Harmon, T. S.; Holehouse, A. S.; Rosen, M. K.; Pappu, R. V. Intrinsically Disordered Linkers Determine the Interplay between Phase Separation and Gelation in Multivalent Proteins. *eLife* **2017**, *6*. https://doi.org/10.7554/eLife.30294.
(39) Shin, Y.; Brangwynne, C. P. Liquid Phase Condensation in Cell Physiology and Disease. *Science* **2017**, *357* (6357), eaaf4382. https://doi.org/10.1126/science.aaf4382.
(40) Banani, S. F.; Lee, H. O.; Hyman, A. A.; Rosen, M. K. Biomolecular Condensates: Organizers of Cellular Biochemistry. *Nat. Rev. Mol. Cell Biol.* **2017**, *18* (5), 285–298. https://doi.org/10.1038/nrm.2017.7.
(41) Badi, N.; Lutz, J.-F. Sequence Control in Polymer Synthesis. *Chem. Soc. Rev.* **2009**, *38* (12), 3383–3390. https://doi.org/10.1039/b806413j.
(42) Lutz, J. F.; Ouchi, M.; Liu, D. R.; Sawamoto, M. Sequence-Controlled Polymers. *SCIENCE* **2013**, *341* (6146), 1238149. https://doi.org/10.1126/science.1238149.
(43) Lutz, J. F.; Lehn, J. M.; Meijer, E. W.; Matyjaszewski, K. From Precision Polymers to Complex Materials and Systems. *Nat. Rev. Mater.* **2016**, *1* (5), UNSP 16024. https://doi.org/10.1038/natrevmats.2016.24.
(44) Jovanovic-Talisman, T.; Tetenbaum-Novatt, J.; McKenney, A. S.; Zilman, A.; Peters, R.; Rout, M. P.; Chait, B. T. Artificial Nanopores That Mimic the Transport Selectivity of the Nuclear Pore Complex. *NATURE* **2009**, *457* (7232), 1023–1027. https://doi.org/10.1038/nature07600.
(45) Hou, X.; Guo, W.; Jiang, L. Biomimetic Smart Nanopores and Nanochannels. *Chem. Soc. Rev.* **2011**, *40* (5), 2385–2401. https://doi.org/10.1039/c0cs00053a.
(46) Tagliazucchi, M.; Szleifer, I. Transport Mechanisms in Nanopores and Nanochannels: Can We Mimic Nature? *Mater. TODAY* **2015**, *18* (3), 131–142. https://doi.org/10.1016/j.mattod.2014.10.020.
(47) Huang, K.; Szleifer, I. Design of Multifunctional Nanogate in Response to Multiple External Stimuli Using Amphiphilic Diblock Copolymer. *J. Am. Chem. Soc.* **2017**, *139* (18), 6422–6430. https://doi.org/10.1021/jacs.7b02057.
(48) Zhang, Z.; Wen, L.; Jiang, L. Bioinspired Smart Asymmetric Nanochannel Membranes. *Chem. Soc. Rev.* **2018**, *47* (2), 322–356. https://doi.org/10.1039/C7CS00688H.
(49) Li, X.; Zhai, T.; Gao, P.; Cheng, H.; Hou, R.; Lou, X.; Xia, F. Role of Outer Surface Probes for Regulating Ion Gating of Nanochannels. *Nat. Commun.* **2018**, *9* (1). https://doi.org/10.1038/s41467-017-02447-7.
(50) Gao, P.; Ma, Q.; Ding, D.; Wang, D.; Lou, X.; Zhai, T.; Xia, F. Distinct Functional Elements for Outer-Surface Anti-Interference and Inner-Wall Ion Gating of Nanochannels. *Nat. Commun.* **2018**, *9* (1). https://doi.org/10.1038/s41467-018-06873-z.
(51) Sun, B.; Kim, Y.; Wang, Y.; Wang, H.; Kim, J.; Liu, X.; Lee, M. Homochiral Porous Nanosheets for Enantiomer Sieving. *Nat. Mater.* **2018**, *17* (7), 599–604. https://doi.org/10.1038/s41563-018-0107-4.
(52) Szleifer, I.; Carignano, M. A. Tethered Polymer Layers. *Adv Chem Phys* **1996**, *94*, 165–260.

(53) Piana, S.; Donchev, A. G.; Robustelli, P.; Shaw, D. E. Water Dispersion Interactions Strongly Influence Simulated Structural Properties of Disordered Protein States. *J. Phys. Chem. B* **2015**, *119* (16), 5113–5123. https://doi.org/10.1021/jp508971m.
(54) Milles, S.; Mercadante, D.; Aramburu, I. V.; Jensen, M. R.; Banterle, N.; Koehler, C.; Tyagi, S.; Clarke, J.; Shammas, S. L.; Blackledge, M.; et al. Plasticity of an Ultrafast Interaction between Nucleoporins and Nuclear Transport Receptors. *Cell* **2015**, *163* (3), 734–745. https://doi.org/10.1016/j.cell.2015.09.047.
(55) Xu, S.; Powers, M. A. In Vivo Analysis of Human Nucleoporin Repeat Domain Interactions. *Mol. Biol. Cell* **2013**, *24* (8), 1222–1231. https://doi.org/10.1091/mbc.e12-08-0585.
(56) Eibauer, M.; Pellanda, M.; Turgay, Y.; Dubrovsky, A.; Wild, A.; Medalia, O. Structure and Gating of the Nuclear Pore Complex. *Nat. Commun.* **2015**, *6*, 7532. https://doi.org/10.1038/ncomms8532.
(57) Ma, J.; Goryaynov, A.; Sarma, A.; Yang, W. Self-Regulated Viscous Channel in the Nuclear Pore Complex. *Proc. Natl. Acad. Sci. U. S. A.* **2012**, *109* (19), 7326–7331. https://doi.org/10.1073/pnas.1201724109.
(58) Tu, L.-C.; Huisman, M.; Chung, Y.-C.; Smith, C. S.; Grunwald, D. Deconstructing Transport-Distribution Reconstruction in the Nuclear-Pore Complex. *Nat. Struct. Mol. Biol.* **2018**, *25* (12), 1061–1062. https://doi.org/10.1038/s41594-018-0161-2.
(59) Sakiyama, Y.; Mazur, A.; Kapinos, L. E.; Lim, R. Y. H. Spatiotemporal Dynamics of the Nuclear Pore Complex Transport Barrier Resolved by High-Speed Atomic Force Microscopy. *Nat. Nanotechnol.* **2016**, *11* (8), 719–+. https://doi.org/10.1038/NNANO.2016.62.
(60) Stanley, G. J.; Fassati, A.; Hoogenboom, B. W. Atomic Force Microscopy Reveals Structural Variability amongst Nuclear Pore Complexes. *Life Sci. Alliance* **2018**, *1* (4), e201800142. https://doi.org/10.26508/lsa.201800142.
(61) Tu, L. C.; Fu, G.; Zilman, A.; Musser, S. M. Large Cargo Transport by Nuclear Pores: Implications for the Spatial Organization of FG-Nucleoporins. *EMBO J.* **2013**, *32* (24), 3220–3230. https://doi.org/10.1038/emboj.2013.239.
(62) Lowe, A. R.; Tang, J. H.; Yassif, J.; Graf, M.; Huang, W. Y.; Groves, J. T.; Weis, K.; Liphardt, J. T. Importin-β Modulates the Permeability of the Nuclear Pore Complex in a Ran-Dependent Manner. *eLife* **2015**, *4*, e04052. https://doi.org/10.7554/eLife.04052.
(63) Kowalczyk, S. W.; Kapinos, L.; Blosser, T. R.; Magalhães, T.; van Nies, P.; Lim, R. Y. H.; Dekker, C. Single-Molecule Transport across an Individual Biomimetic Nuclear Pore Complex. *Nat. Nanotechnol.* **2011**, *6* (7), 433–438. https://doi.org/10.1038/nnano.2011.88.
(64) Ma, J.; Goryaynov, A.; Yang, W. Super-Resolution 3D Tomography of Interactions and Competition in the Nuclear Pore Complex. *Nat. Struct. Mol. Biol.* **2016**, *23* (3), 239–247. https://doi.org/10.1038/nsmb.3174.
(65) Tagliazucchi, M.; Huang, K.; Szleifer, I. Routes for Nanoparticle Translocation through Polymer-Brush-Modified Nanopores. *J. Phys. Condens. Matter* **2018**, *30* (27), 274006. https://doi.org/10.1088/1361-648X/aac90b.
(66) Colwell, L. J.; Brenner, M. P.; Ribbeck, K. Charge as a Selection Criterion for Translocation through the Nuclear Pore Complex. *PLOS Comput. Biol.* **2010**, *6* (4), e1000747. https://doi.org/10.1371/journal.pcbi.1000747.
(67) Fiserova, J.; Richards, S. A.; Wente, S. R.; Goldberg, M. W. Facilitated Transport and Diffusion Take Distinct Spatial Routes through the Nuclear Pore Complex. *J. Cell Sci.* **2010**, *123* (16), 2773–2780. https://doi.org/10.1242/jcs.070730.
(68) Ma, J.; Yang, W. Three-Dimensional Distribution of Transient Interactions in the Nuclear Pore Complex Obtained from Single-Molecule Snapshots. *Proc. Natl. Acad. Sci.* **2010**, *107* (16), 7305–7310. https://doi.org/10.1073/pnas.0908269107.
(69) Curk, T.; Dobnikar, J.; Frenkel, D. Optimal Multivalent Targeting of Membranes with Many Distinct Receptors. *Proc. Natl. Acad. Sci.* **2017**, *114* (28), 7210–7215. https://doi.org/10.1073/pnas.1704226114.
(70) Onischenko, E.; Tang, J. H.; Andersen, K. R.; Knockenhauer, K. E.; Vallotton, P.; Derrer, C. P.; Kralt, A.; Mugler, C. F.; Chan, L. Y.; Schwartz, T. U.; et al. Natively Unfolded FG Repeats Stabilize the Structure of the Nuclear Pore Complex. *Cell* **2017**, *171* (4), 904-917.e19. https://doi.org/10.1016/j.cell.2017.09.033.
(71) Ma, J.; Liu, Z.; Michelotti, N.; Pitchiaya, S.; Veerapaneni, R.; Androsavich, J. R.; Walter, N. G.; Yang, W. High-Resolution Three-Dimensional Mapping of MRNA Export through the Nuclear Pore. *Nat. Commun.* **2013**, *4* (1). https://doi.org/10.1038/ncomms3414.
(72) Isgro, T. A.; Schulten, K. Binding Dynamics of Isolated Nucleoporin Repeat Regions to Importin-β. *Structure* **2005**, *13* (12), 1869–1879. https://doi.org/10.1016/j.str.2005.09.007.
(73) Timney, B. L.; Raveh, B.; Mironska, R.; Trivedi, J. M.; Kim, S. J.; Russel, D.; Wente, S. R.; Sali, A.; Rout, M. P. Simple Rules for Passive Diffusion through the Nuclear Pore Complex. *J. CELL Biol.* **2016**, *215* (1), 57–76. https://doi.org/10.1083/jcb.201601004.

(74) Simon, S. M.; Peskin, C. S.; Oster, G. F. What Drives the Translocation of Proteins? *Proc. Natl. Acad. Sci.* **1992**, *89* (9), 3770–3774. https://doi.org/10.1073/pnas.89.9.3770.
(75) Mincer, J. S.; Simon, S. M. Simulations of Nuclear Pore Transport Yield Mechanistic Insights and Quantitative Predictions. *Proc. Natl. Acad. Sci.* **2011**, *108* (31), E351–E358. https://doi.org/10.1073/pnas.1104521108.
(76) Strawn, L. A.; Shen, T.; Shulga, N.; Goldfarb, D. S.; Wente, S. R. Minimal Nuclear Pore Complexes Define FG Repeat Domains Essential for Transport. *Nat. Cell Biol.* **2004**, *6* (3), 197–206. https://doi.org/10.1038/ncb1097.

Figure 1. Basic input and output of the model. (**A**) IDR sequences with colored markers corresponding to different types of FG repeats and spacers. The names and stoichiometry of the FG-Nups are listed to the left of the anchoring ends of the sequences. Schematic representations of the three types of FG motifs are shown under the sequences. Spheres indicate hydrophilic and ovals hydrophobic amino acids. (**B**) Geometry of the model NPC. The scaffold rings are coarse-grained into three tori. On the right, the anchor positions of the IDRs are represented by colored discs (disc size indicates the length of the sequence). On the left, the color of the anchor position aligns with the color code of the dominating FG-type of the IDR (colored orange if there is no dominant FG-type). Triangles indicate cohesive IDRs, squares non-cohesive and Nsp1. (**C**) Color map of the mM concentration of all the amino acids inside the NPC with 2.5 kT FG pairing interaction and 1kT cohesive spacer attraction. The vestibular condensates are marked by the dashed circles with the cytoplasmic one on the top. (**D-H**) Structural dependence of the central channel on protein interactions is shown in the grey panels with the FG-pairing strength and cohesive spacer attraction strength displayed in the left and the right, respectively.

Figure 2. FG and electrostatic profiles inside the nuclear pore. (**A**) Overall FG concentration throughout the NPC in mM. (**B**) FG-pairing fraction in percentage. (**C**) Concentration of NQT (neutral and cohesive) spacers in mM. (**D**) Concentration of net IDR charge in mM. (**E**) Electrostatic potential throughout the NPC in mV. (**F**) Concentration of DEKR (charged and non-cohesive) spacers in mM.

Figure 3. Distinct domains of different FG motifs and of cohesive and non-cohesive FG-Nups. (**A-C**) Spatial distributions of three generic types of FG motifs (see main text for the classification protocol). (**D-F**) Spatial distributions of non-GLFG-FxFG (including type-1) motifs, GLFG (belonging to type-2) motifs, and FxFG (belonging to type-3) motifs. Note that panel D has different concentration scale than panels E, F. (**G-I**) Spatial distributions of cohesive FG-Nups (Nup116, Nup100, Nup42, Nup57, Nup49, Nup145N), non-cohesive FG-Nups (Nup159, Nup1, Nup2, Nup60) and Nsp1 (partially cohesive). All the color maps show amino-acid concentrations in mM.

Figure 4. An atlas of various FG-Nups of yeast NPC shown in color maps. From top to bottom, the three rows show the spatial distributions of the FG-Nups with their anchor positions located towards the cytoplasm, near the central inner ring, and towards the nucleoplasm. The copy number of each individual Nup is indicated in the parenthesis.

Figure 5. Reference system of non-interacting FG-Nups. (**A**) Superposition of all 11 IDRs (large panel) and 4 typical individual IDRs (small panels). (**B-I**) Spatial distributions of NQT spacers (B), charged DEKR spacers (C), net charge of IDR amino acids (D), electrostatic potential (E), all FG motifs (F), type-1 FG motifs (G), type-2 FG motifs (H) and type-3 FG motifs.

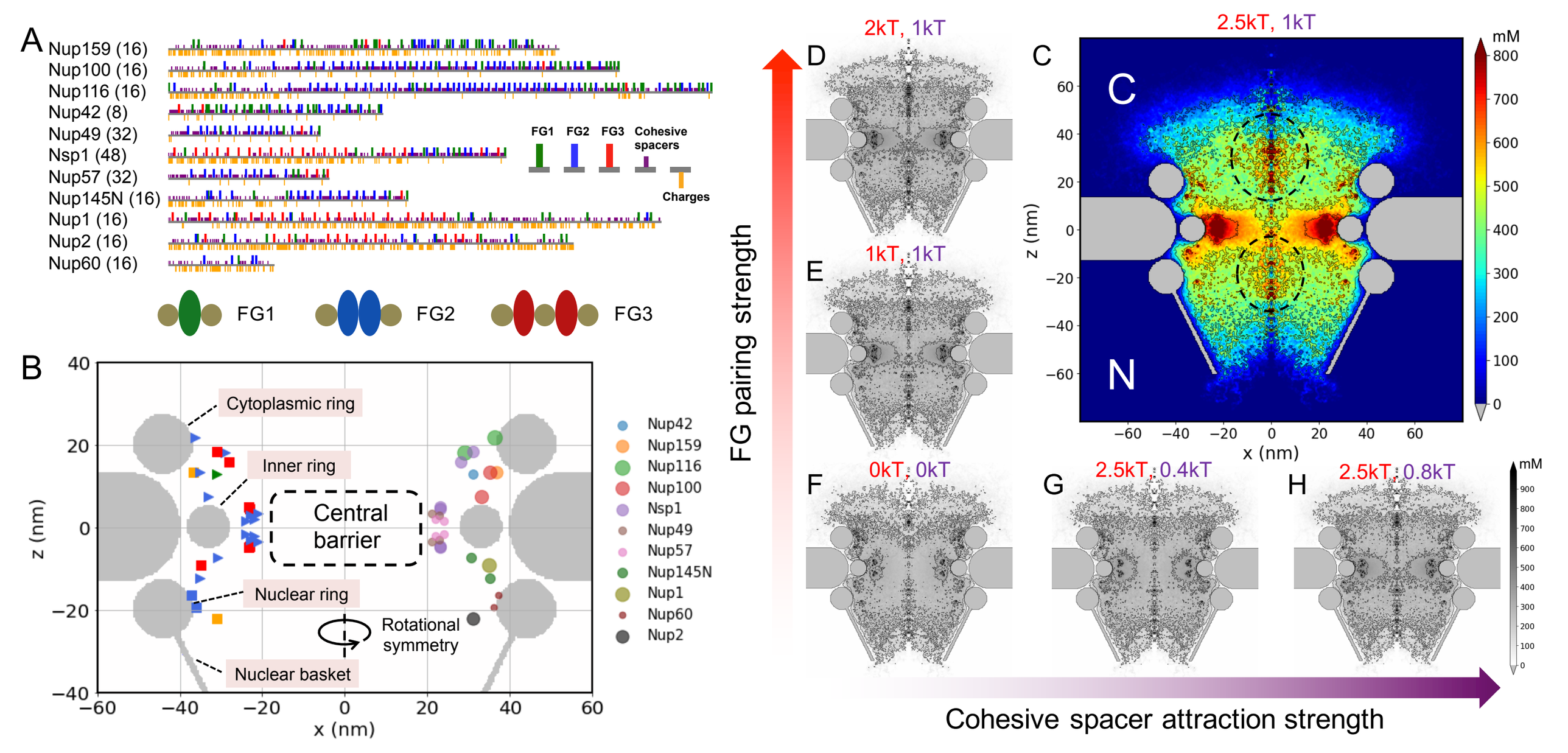
A
Nup159 (16)
Nup100 (16)
Nup116 (16)
Nup42 (8)
Nup49 (32)
Nsp1 (48)
Nup57 (32)
Nup145N (16)
Nup1 (16)
Nup2 (16)
Nup60 (16)
FG1
FG2
FG3
Cohesive spacers
Charges
FG1
FG2
FG3
B
Cytoplasmic ring
Inner ring
Central barrier
Nuclear ring
Rotational symmetry
Nuclear basket
z (nm)
x (nm)
Nup42
Nup159
Nup116
Nup100
Nsp1
Nup49
Nup57
Nup145N
Nup1
Nup60
Nup2
FG pairing strength
2kT, 1kT
D
1kT, 1kT
E
0kT, 0kT
F
2.5kT, 1kT
C
C
N
z (nm)
x (nm)
mM
2.5kT, 0.4kT
G
2.5kT, 0.8kT
H
Cohesive spacer attraction strength

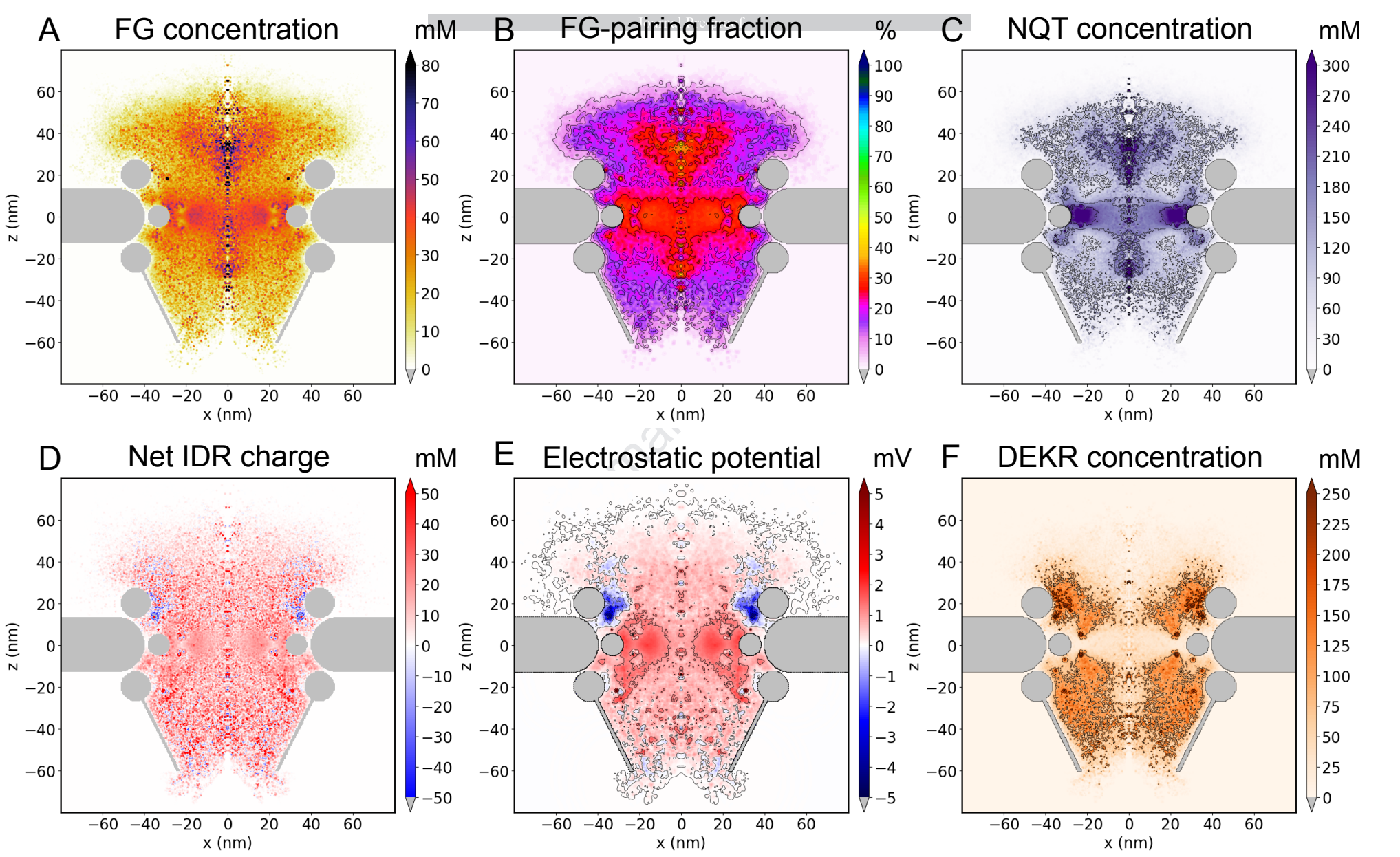
A
FG concentration
mM
B
FG-pairing fraction
%
C
NQT concentration
mM
D
Net IDR charge
mM
E
Electrostatic potential
mV
F
DEKR concentration
mM
z (nm)
x (nm)

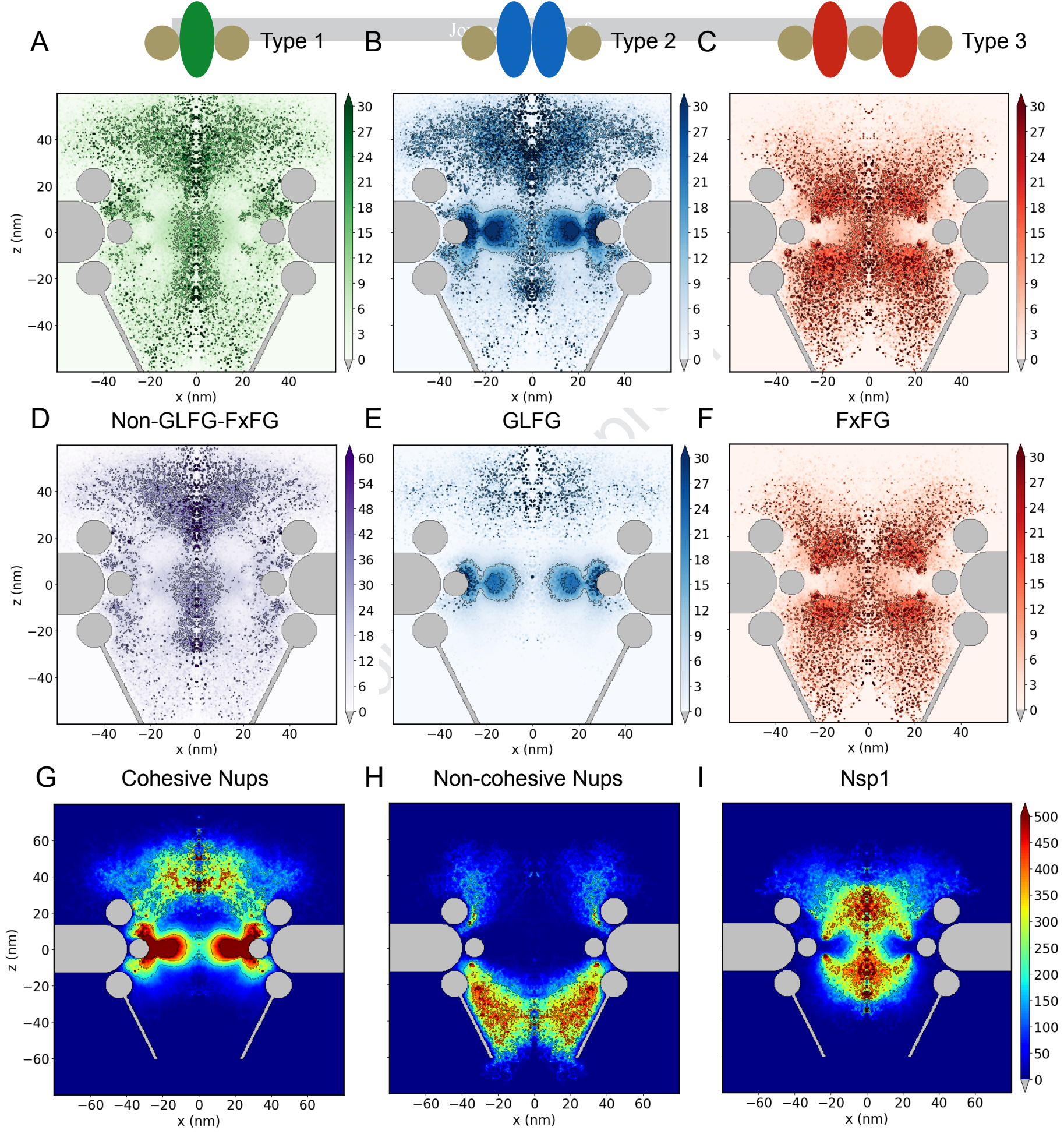
A
Type 1
B
Type 2
C
Type 3
D
Non-GLFG-FxFG
E
GLFG
F
FxFG
G
Cohesive Nups
H
Non-cohesive Nups
I
Nsp1
z (nm)
x (nm)

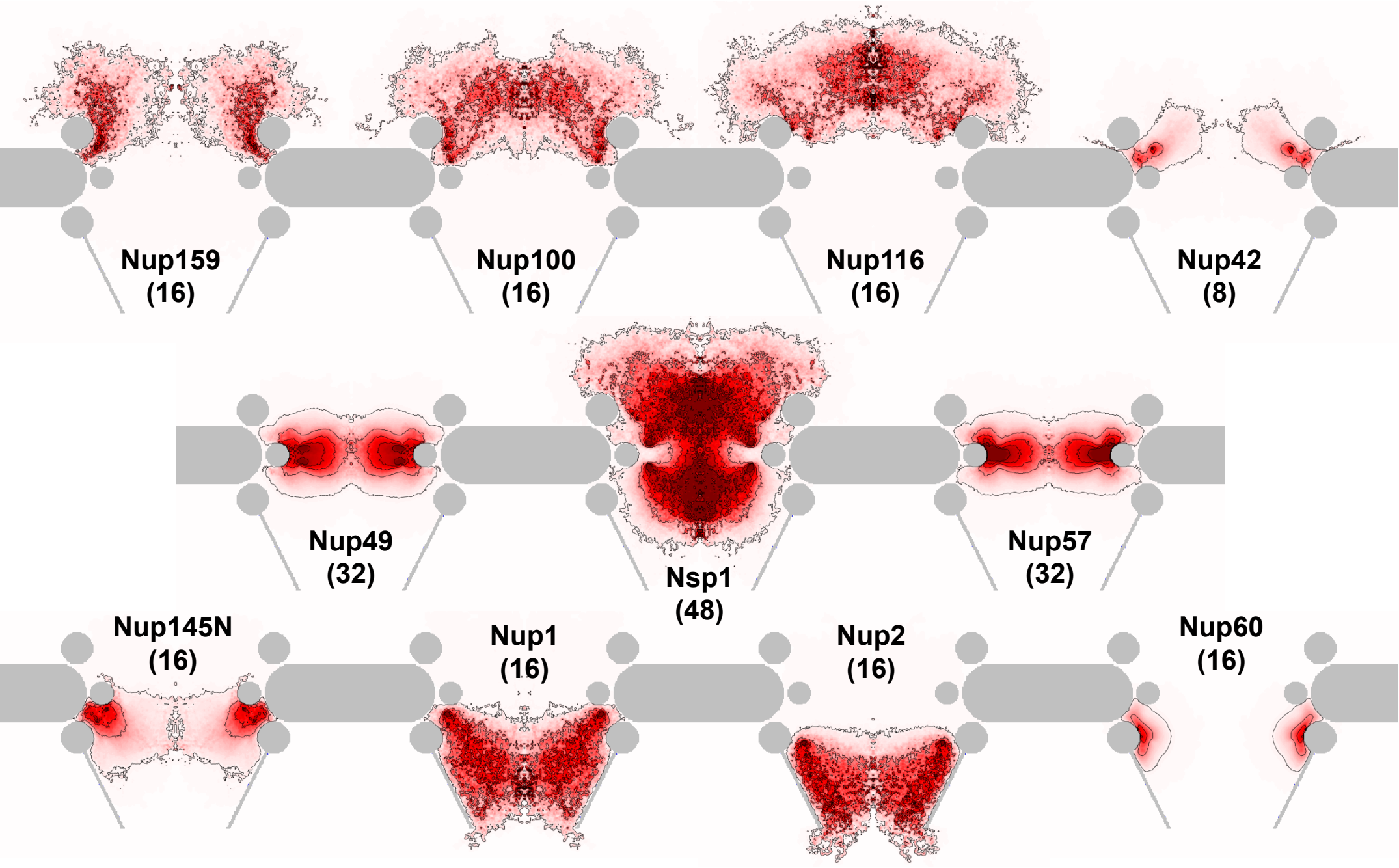
Nup159
(16)
Nup100
(16)
Nup116
(16)
Nup42
(8)
Nup49
(32)
Nsp1
(48)
Nup57
(32)
Nup145N
(16)
Nup1
(16)
Nup2
(16)
Nup60
(16)

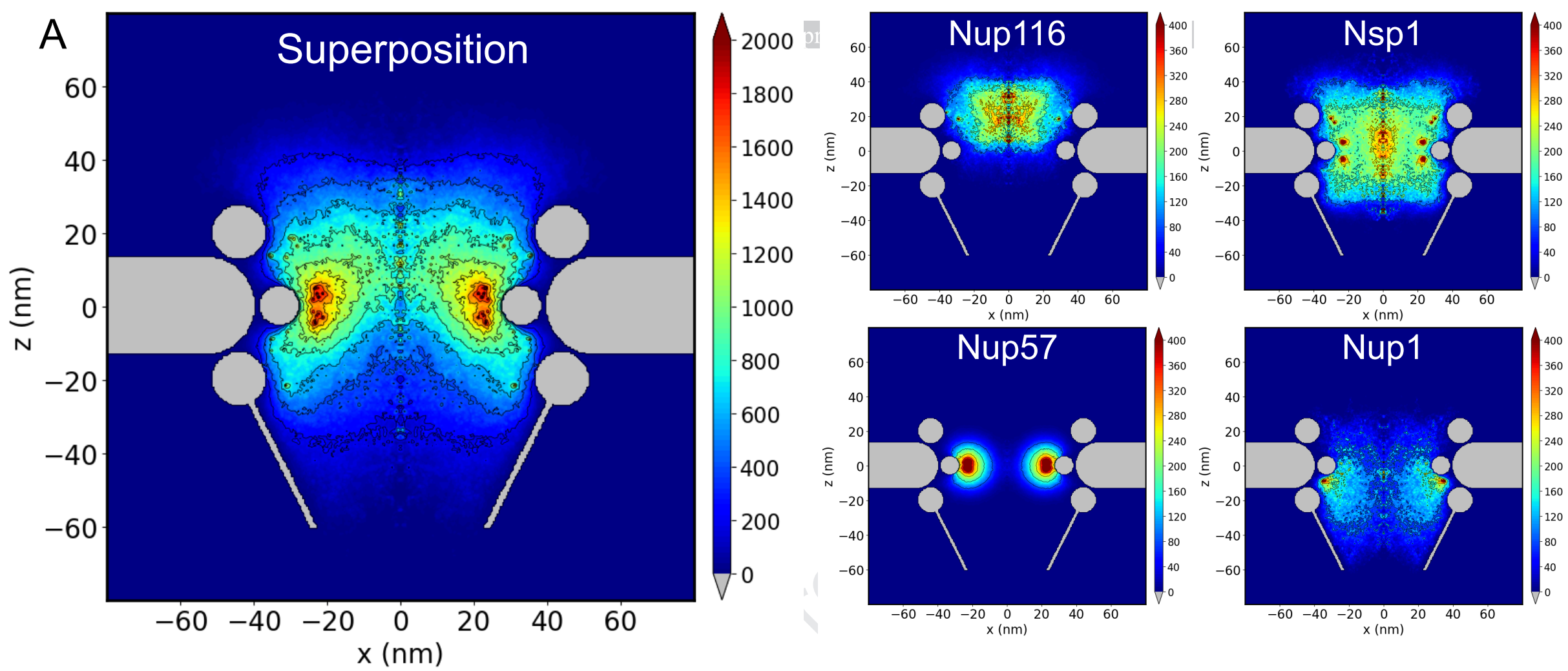
A
Superposition
Nup116
Nsp1
Nup57
Nup1
z (nm)
x (nm)
NQT spacers
DEKR spacers
IDRs net charge
Electrostatic potential
B
C
D
E
All FG
Type-1 FG
Type-2 FG
Type-3 FG
F
G
H
I